# Solute misfit and solute interaction effects on strengthening: a case study in AuNi

Binglun Yin[a,∗], Linhan Li[a], Sophie Drescher[b], Sascha Seils[c,d], Shankha Nag[e,f], Jens Freudenberger[b], W. A. Curtin[e]

[a]*Institute of Applied Mechanics and Center for X-Mechanics, Zhejiang University, 310027 Hangzhou, China*
[b]*Leibniz Institute for Solid State and Materials Research, 01069 Dresden, Germany*
[c]*Institute for Applied Materials (IAM-WK), Karlsruhe Institute of Technology (KIT), 76131 Karlsruhe, Germany*
[d]*Karlsruhe Nano Micro Facility (KNMFi), Karlsruhe Institute of Technology (KIT), 76344 Eggenstein-Leopoldshafen, Germany*
[e]*Laboratory for Multiscale Mechanics Modeling (LAMMM), École Polytechnique Fédérale de Lausanne, 1015 Lausanne, Switzerland*
[f]*Institute for Materials Science, Technical University of Darmstadt, 64287 Darmstadt, Germany*

## Abstract

AuNi is a classic long-studied fcc alloy combining a very "large" atom (Au) and a very "small" atom (Ni), and the large atomic size misfits suggest very high strengthening. Here, AuNi is used as a model alloy for the testing of new strengthening theories in random alloys that include the effects of both size misfits and solute-solute interactions. Experimentally, AuNi samples are fabricated, characterized, and tested, and show no segregation after annealing at 900 °C and a very high yield strength of 769 MPa. Theoretically, the main inputs to the theory (alloy lattice and elastic constants, solute misfit volumes, energy fluctuations associated with slip in the presence of solute-solute interactions) are extracted from experiments or computed using first-principles DFT. The parameter-free prediction of the yield strength is 809 MPa, in very good agreement with experiments. Solute-solute interactions enhance the strength only moderately (13%), demonstrating that the strengthening is dominated by the solute misfit contribution. Various aspects of the full theory are discussed, the general methodology is presented in an easy-to-apply analytic framework, and a new analysis for strengthening in alloys with zero misfits but non-zero solute-solute interactions is presented. These results provide support for the theories and point toward applications to many fcc complex concentrated alloys.

*Keywords:* yield strength, solute strengthening theory, misfit volume, stacking fault energy

## 1. Introduction

The development of high-performance structural metal alloys has been rejuvenated by the discovery of high-entropy alloys (HEAs) [1, 2]. In contrast to conventional metallic alloys that have only one major element, complex concentrated alloys (CCAs) [3, 4] including HEAs consist of multi-principal elements at non-dilute compositions, providing a high-dimensional composition space with immense possibilities for alloy optimization. Probing that vast space is facilitated by theories that can accurately predict alloy properties in terms of accessible/computable underlying alloy properties.

The prevailing theory for random alloy yield strength at experimental temperatures and strain rates is based on solute strengthening, for both CCAs [5, 6] and dilute alloys [7, 8]. Using an elasticity approximation, the theory depends primarily on solute misfit volumes in the alloy and alloy elastic constants. In fcc metals, the theory shows that dislocation dissociation distance $d_{\text{partial}}$ plays a very limited role if $d_{\text{partial}} > 6.5b$ ($b$ the Burgers vector) so that an analytic theory is broadly applicable [9]. The theory has been shown to predict the experimental yield strengths with good accuracy ($\pm 15\%$) in the Cantor alloy family (Co-Cr-Fe-Ni-Mn) [10–12], noble metal alloys [9, 13], and the Cantor alloys with additions of Vanadium [14] or Palladium [15]. The latter CoCrFeNiPd alloy is interesting because the random alloy theory agrees with the high measured strength, relative to CoCrFeNiMn, even though the alloy has some local ordering [16]. Thus, any future predictions of CoCrFeNiPd using any theory that includes any ordering effects would have to predict the same experiments, implying that ordering does not necessarily enhance strength above that of the random state.

Although many successes of the random alloy solute strengthening theory have been reported, the theory neglects the effects of direct solute-solute interactions. Solute-solute interactions are the underlying

---

∗Corresponding author
*Email address:* binglun.yin@zju.edu.cn (Binglun Yin)

driving force for the formation of short-range order (SRO), phase separation, or precipitation, with consequent effects on strengthening [17]. But even in the random alloy, solute-solute interactions create an additional source of energetic fluctuations as a dislocation glides and this leads to extra strengthening. The inclusion of solute-solute interactions into the strengthening theory for random alloys has been recently developed [18]. The extended theory requires the intrinsic energy fluctuations $\widetilde{\sigma}_{\Delta U_{s-s}}$ associated with slip in the presence of solute-solute interactions. Determining this quantity is non-trivial, so the extended theory has thus not yet been widely applied.

Here, we aim to test the above strengthening theories in a well-characterized model alloy. To reduce the complexity, it is useful to first carry out investigations on a simple concentrated alloy system, and the AuNi fcc binary alloy is an excellent choice for this purpose. Au-Ni system has a simple phase diagram [19], i.e. a homogeneous fcc solid solution within the entire concentration range at high temperatures $T \approx 1090$–$1220$ K (homogeneity being a prerequisite for applying the theory), phase separation into Au-rich and Ni-rich fcc phases below $T \approx 1090$ K (which is a high $T$ and indicates strong solute-solute interactions), and no ordered intermetallics down to at least $T = 400$ K. Furthermore, Au and Ni have a very large size difference, relative to many other fcc elements, generating large misfits at the 50–50 composition. Hence, AuNi should have a high yield strength due to the large misfits as well as the solute-solute interactions. To apply the extended theory to AuNi, we compute $\widetilde{\sigma}_{\Delta U_{s-s}}$ using Density Functional Theory (DFT) by directly sampling the stacking fault (SF) energies in the random alloy. To ensure that we compare theory to a well-characterized alloy, we also fabricate, characterize, and test the AuNi alloy. The predicted alloy strength is in good agreement with the measured value, and the strength enhancement due to solute-solute interactions is moderate. Hence, the strengthening is dominated by the solute misfit volumes, consistent with much of the previous success of the misfit-only theory.

The remainder of this paper is organized as follows. In Section 2, we first present the details related to the processing, characterization, and performance of the AuNi alloy. In Section 3, we summarize the solute strengthening theory extended to include solute-solute interactions. In Section 4, we present the calculations of the inputs required by the theory. We then make strength predictions for the random AuNi alloy in Section 5, based on the results of Sections 3 and 4. We discuss various implications of the theory in Section 6.

We summarize our work in Section 7.

## 2. Experiments on AuNi

### 2.1. Sample preparation and methods

A polycrystalline AuNi sample is prepared from pure elements (purity: 4N, Au from AGOSI, Ni from Alfa Aeser) by arc-melting with a setting pressure of 0.7 bar Ar. In order to obtain homogeneous material, the samples are turned over and re-melted four times with a time of 30 s. After the last melting step, the samples are suction cast into a copper mold with a diameter of 4 mm and a length of 75 mm. The as-cast alloy is homogenized at 900 °C for 20 h. In order to obtain a well-defined microstructure the samples are rotary swaged to a diameter of 2.8 mm with an areal reduction of ∼ 20% per step, and subsequently recrystallized at 900 °C for 1 h, followed by water-quenching.

The phase purity of AuNi is proven by X-ray diffractometry. The lattice parameter is determined from the measured diffraction pattern utilizing the Fullprof Rietveld program [20]. Structural characterization was done by X-ray diffraction in Debye-Scherrer geometry on bulk samples with a thickness below 30 $\mu$m utilizing a STOE STADI_P diffractometer with MoK$_{\alpha 1}$ radiation (0.70932 nm) equipped with a position sensitive detector Dectris Mythen 1K and a curved Ge(111)-monochromator. The scans are taken from $2\theta = 15°$ up to 60° in steps of 0.01°.

The texture of AuNi is determined from X-ray analysis. For this purpose, a Panalytical X'pert PW3040 diffractometer is applied. The diffractometer uses CuK$_{\alpha 1}$ radiation (1.544332 nm) and is equipped with a four-circle goniometer. (111), (200), (220), and (311) pole figures are examined.

Atom probe tomography (APT) is utilized to evaluate the elemental distribution after recrystallization. The investigated sample is prepared from a volume without any grain boundaries with a FIB FEI Strata, utilizing the standard lift-out method on a microtip coupon. The analysis is performed with a local electrode atom probe (LEAP 4000X HR, Cameca) at a temperature of about 50 K with a pulse frequency of 125 kHz and a pulse energy of 50 pJ. The reconstructed tip consists of approximately $13 \times 10^6$ ions. The Cameca software IVAS 3.6.14 is used to evaluate the APT results.

Mechanical tests are performed in compression utilizing an electro-mechanical Instron 8562 testing machine with constant crosshead movement corresponding to an initial strain rate of $10^{-3}$ s$^{-1}$, at room temperature. The samples possess an initial diameter = 2.8 mm and height
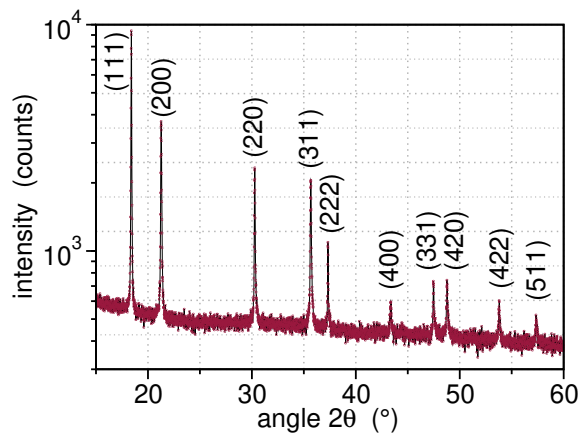
Figure 1: X-ray diffraction pattern of AuNi samples in the recrystallized state.
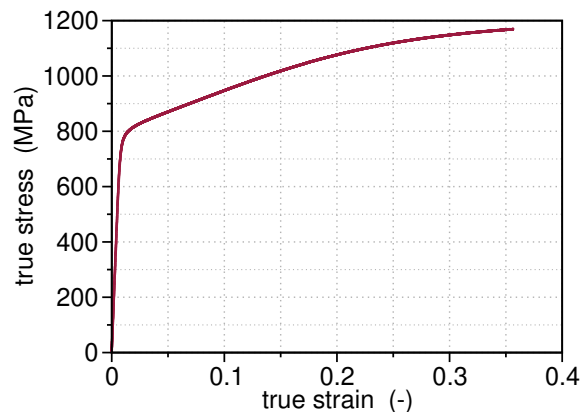


Figure 3: True compressive stress-strain curve of AuNi samples in the recrystallized state. Only one curve is shown since all four curves fall on each other and are hard to separate.

⩽ 5.4 mm. The tests are stopped when the aspect ratio approaches height/diameter = 1.

### 2.2. Experimental results

Characterization and testing of the recrystallized AuNi samples reveal the following results. The X-ray diffraction pattern is shown in Fig. 1 and reveals a single fcc phase without the presence of any secondary phases nor any phase decomposition. The lattice parameter of AuNi is determined as $a = 3.840 \pm 0.004$ Å at room temperature.

The texture analysis of AuNi in the recrystallized state does not exhibit any preferred orientation. The pole figures (not shown) reveal that the individual crystallizes have a random distribution of their orientations. The grain size in the recrystallized samples is determined as ~ 60 $\mu$m from SEM micrographs with the line intersection method.
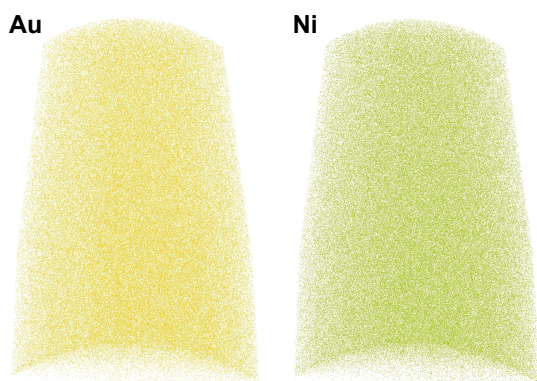


Figure 2: Atom probe tomography (APT) results of AuNi samples in the recrystallized state (900 °C for 1 hour).

With the help of APT, the three-dimensional elemental distributions are examined, as shown in Fig. 2, which appear homogeneous. In order to provide a clear view of the elemental distribution, only 3% of all ions are visualized here. This does not alter the finding that AuNi samples show no segregation at the atomic scale, consistent with the phase diagram. Despite the possible existence of SRO, it is reasonable to start with random alloy theories to understand and predict the initial yield strength of the AuNi alloy.

The compression tests on four samples reveal a yield strength of 769 ± 4 MPa, as shown in Fig. 3. The samples are ductile and did not fail until the height/diameter = 1 (criterion for ending the compression test) was met. Recognizing the large uncertainty of determining Young's modulus in compression mode, a rough estimate for this property is 101 ± 8 GPa.

## 3. Solute strengthening theory in random alloys

### 3.1. General framework

The yield strength of fcc single-phase alloys has been broadly understood as due to solid solution strengthening that arises from the collective interactions of all of the essentially randomly distributed atoms with dislocations [5, 21, 22]. In random alloys, the dislocation becomes wavy to minimize the total energy, which has contributions from the interactions (fluctuations that decrease the energy) and line tension Γ (increasing the energy). In the minimum energy state, the wavy configuration can be characterized by a wavelength $4\zeta_c$ and amplitude $w_c/2$. Segments of length $\zeta_c$ are thus trapped in local energetically-favorable environments and face

**(a)** Waviness of a long dislocation



**(b)** Energy barrier for dislocation segment $\zeta_c$



$$E(x) = \frac{\Delta E_b}{2}\left[1 - \cos\frac{\pi x}{w_c}\right]$$
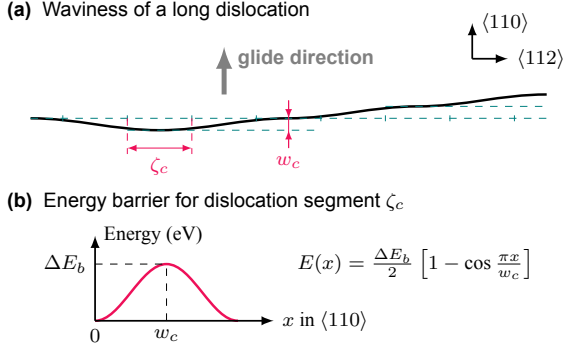
Figure 4: Schematics of the characteristic lengths of a long wavy dislocation and the energy landscape for dislocation segment $\zeta_c$ in the stress- and temperature-assisted glide.

barriers of magnitude $\Delta E_b$ created by energetically-unfavorable environments at a distance $w_c$, as illustrated in Fig. 4. A combination of stress and temperature is then required for the segments to overcome the barriers and cause plastic flow, leading to a temperature- and strain-rate-dependent yield stress. In the following, we present the key equations of the theory for completeness and clarity.

The general theory starts with the analysis of the total energy change $\Delta U_{\text{tot}}(\zeta, w)$ when a dislocation segment of length $\zeta$ glides by a distance of $w$ through the random solute field. Then the quantity of importance is the standard deviation of $\Delta U_{\text{tot}}(\zeta, w)$, i.e., $\sigma_{\Delta U_{\text{tot}}}(\zeta, w)$. When specialized to dissociated dislocations with partial separation $d_{\text{partial}} > w$, $\sigma_{\Delta U_{\text{tot}}}(\zeta, w)$ can be written as

$$\sigma_{\Delta U_{\text{tot}}}(\zeta, w) = \left[\frac{\zeta}{\sqrt{3}b}\right]^{\frac{1}{2}} \underbrace{\sqrt{\Delta\widetilde{E}_{p,s-d}^2(w) + 2\frac{2w}{b}\widetilde{\sigma}_{\Delta U_{s-s}}^2}}_{\Delta\widetilde{E}_p(w)}.$$

$$(1)$$

Here, $\Delta\widetilde{E}_{p,s-d}(w)$ is the normalized energy fluctuation due to solute-dislocation interactions, $\widetilde{\sigma}_{\Delta U_{s-s}}$ is the normalized energy fluctuation associated with Shockley partial slip in the presence of solute-solute interactions, and $b = a/\sqrt{2}$ is the dislocation Burgers vector. The derivations of Eq. 1 can be found in Ref. [18].

With the definition of $\sigma_{\Delta U_{\text{tot}}}(\zeta, w)$, the parameter-free solute strengthening model as originally proposed by Leyson et al. [7] can be revisited as follows. For a long straight dislocation with total length $L$, the total energy change upon becoming wavy at scales $(\zeta, w)$ is

$$\Delta E_{\text{tot}}(\zeta, w) = \left[\Gamma\frac{w^2}{2\zeta} - \sigma_{\Delta U_{\text{tot}}}(\zeta, w)\right]\frac{L}{2\zeta}. \qquad (2)$$

Minimization of $\Delta E_{\text{tot}}(\zeta, w)$ determines the characteristic lengths $\zeta_c$ and $w_c$. Minimization with respect to $\zeta$ is analytic and yields

$$\zeta_c(w) = \left[4\sqrt{3}\frac{\Gamma^2 w^4 b}{\Delta\widetilde{E}_p^2(w)}\right]^{\frac{1}{3}}. \qquad (3)$$

Minimization with respect to $w$ then reduces to

$$\frac{\partial\Delta\widetilde{E}_{p,s-d}(w)}{\partial w} = \frac{\Delta\widetilde{E}_{p,s-d}(w)}{2w}, \qquad (4)$$

which only involves $\Delta\widetilde{E}_{p,s-d}(w)$. Hence, $w_c$ is independent of the solute-solute interactions. This is fortunate because it enables easy extension of the misfit-only theory to include solute-solute interactions, as presented below. With the characteristic scales $(\zeta_c, w_c)$ determined, the energy barrier $\Delta E_b$ and the zero-temperature shear yield stress $\tau_{y0}$ can be expressed as

$$\Delta E_b = 1.22\left[\frac{\Gamma w_c^2 \Delta\widetilde{E}_p^2(w_c)}{b}\right]^{\frac{1}{3}},$$
$$\tau_{y0} = 1.01\left[\frac{\Delta\widetilde{E}_p^4(w_c)}{\Gamma b^5 w_c^5}\right]^{\frac{1}{3}}. \qquad (5)$$

The uniaxial yield strength for polycrystals at finite temperature $T$ and loading strain rate $\dot{\varepsilon}$ is then obtained via standard thermal activation theory as

$$\sigma_y(T, \dot{\varepsilon}) = 3.06\tau_{y0}\left[1 - \left(\frac{kT}{\Delta E_b}\ln\frac{\dot{\varepsilon}_0}{\dot{\varepsilon}}\right)^{\frac{2}{3}}\right], \qquad (6)$$

where 3.06 is the Taylor factor for untextured fcc polycrystals and $\dot{\varepsilon}_0 = 10^4$ s$^{-1}$ is a reference strain rate.

### 3.2. Analytical model

The analytical application of the extended theory starts with only the solute-dislocation interactions, i.e. assuming $\widetilde{\sigma}_{\Delta U_{s-s}} = 0$. We consider an $N$-component alloys with composition $\{c_n\}$, $n = 1...N$. $\Delta\widetilde{E}_{p,s-d}(w)$ arises due to the solute-dislocation interaction energies $U_n(\boldsymbol{x}_i)$ for a type-$n$ solute at site-$i$ with position $\boldsymbol{x}_i$ relative to the dislocation at the origin lying along the $z$ axis. To obtain an analytic form, we first approximate the interaction energy using elasticity theory as $U_n(\boldsymbol{x}_i) = -p(\boldsymbol{x}_i)\Delta V_n$, where $p(\boldsymbol{x}_i)$ is the dislocation pressure field at position $\boldsymbol{x}_i$ and $\Delta V_n$ is the misfit volume of the type-$n$ solute in the alloy. In this form, the role of dislocation core structure (partial separation $d_{\text{partial}}$ and partial core width $\sigma_{\text{partial}}$) is isolated from the details of the solute misfit

4

volumes and elastic constants. For $d_{\text{partial}} > 6.5b$ and $\sigma_{\text{partial}} = 1.5b$ (a typical value for fcc metals), the effects of the core structure are constants, denoted as $A_E$ and $A_\tau$ in the following. The resulting analytic form for the barrier and strength is thus

$$\Delta E_{b,s-d} = A_E \left[\frac{\Gamma}{b^2}\right]^{\frac{1}{3}} b^3 \left[\mu^V \frac{1 + \nu^V}{1 - \nu^V}\right]^{\frac{2}{3}} \delta^{\frac{2}{3}}$$

$$\tau_{y0,s-d} = A_\tau \left[\frac{\Gamma}{b^2}\right]^{-\frac{1}{3}} \left[\mu^V \frac{1 + \nu^V}{1 - \nu^V}\right]^{\frac{4}{3}} \delta^{\frac{4}{3}}. \tag{7}$$

Here, $\delta = \sqrt{\sum_n c_n \Delta V_n^2}/\left(3V_{\text{alloy}}\right)$ is the well-known $\delta$-parameter describing the collective effect of misfit volumes and $V_{\text{alloy}} = a^3/4$ for fcc alloys. $\mu^V$ and $\nu^V$ are the Voigt average shear modulus and Poisson's ratio of the alloy, which best represent the effects of the fully anisotropic dislocation pressure field [23]. The numerical factors $A_E = 2.5785 \left[1 - (A - 1)/80\right]$ and $A_\tau = 0.04865 \left[1 - (A - 1)/40\right]$ are predetermined with a small elastic anisotropy correction in terms of the Zener anisotropy index $A = 2C_{44}/(C_{11} - C_{12})$. Finally, the dislocation line tension is approximated as $\Gamma = 0.125\mu_{110/111}b^2$ where $\mu_{110/111} = (C_{11} - C_{12} + C_{44})/3$ is the shear modulus for fcc slip on the {111} plane in the $\langle 110 \rangle$ direction. This form of the strengthening model is thus fully analytic, involves only underlying material properties, and has no fitting parameters. The relevant derivations of Eq. 7 can be found in Refs. [5, 9, 24].

In addition to strength, the key quantities in the general theory can also be back-calculated from the analytic results as

$$w_c/b = 0.877 \left[A_E^{\frac{2}{3}} A_\tau^{-\frac{1}{3}}\right] \approx 4.52,$$

$$\Delta \widetilde{E}_{p,s-d}(w_c) = 0.845 \left[A_E^{\frac{5}{6}} A_\tau^{\frac{1}{3}}\right] b^3 \left[\mu^V \frac{1 + \nu^V}{1 - \nu^V}\right] \delta. \tag{8}$$

Here, $w_c/b$ turns out to be very weakly dependent on the elastic anisotropy and so is essentially constant, as indicated. $w_c$ also satisfies the requirement $w_c < d_{\text{partial}}$ (for Eq. 1) in the domain $d_{\text{partial}} > 6.5b$ where the coefficients in Eq. 7 apply.

We now include the solute-solute interactions as represented through the quantity $\widetilde{\sigma}_{\Delta U_{s-s}}$ appearing in Eq. 1. Since $w_c$ remains unchanged as mentioned above, $\Delta \widetilde{E}_p(w_c)$ can be calculated immediately based on the misfit-only fluctuation $\Delta \widetilde{E}_{p,s-d}$ and the material parameter $\widetilde{\sigma}_{\Delta U_{s-s}}$. The formalism of Eq. 5 then allows the calculation of $\Delta E_b$ and $\tau_{y0}$ as

$$\frac{\Delta E_b}{\Delta E_{b,s-d}} = \left[\frac{\Delta \widetilde{E}_p(w_c)}{\Delta \widetilde{E}_{p,s-d}(w_c)}\right]^{\frac{2}{3}} = \left[1 + R_{ss/sd}^2\right]^{\frac{1}{3}},$$

$$\frac{\tau_{y0}}{\tau_{y0,s-d}} = \left[\frac{\Delta \widetilde{E}_p(w_c)}{\Delta \widetilde{E}_{p,s-d}(w_c)}\right]^{\frac{4}{3}} = \left[1 + R_{ss/sd}^2\right]^{\frac{2}{3}}, \tag{9}$$

where the ratio $R_{ss/sd} \approx \frac{4.25\widetilde{\sigma}_{\Delta U_{s-s}}}{\Delta \widetilde{E}_{p,s-d}(w_c)}$ reflects the relative importance of solute-solute and solute-dislocation energy fluctuations.

The inclusion of solute-solute interactions increases both the energy barrier and the zero-temperature shear yield stress. However, the effects of the solute-solute interactions enter only through the square of the ratio $R_{ss/sd}$, making them of reduced importance if the solute-dislocation energy fluctuations are high. The final uni-axial yield strength including solute-solute interactions is then easily computed via Eq. 6.

Overall, the application of the extended theory requires the alloy lattice and elastic constants, the solute misfit volumes, and $\widetilde{\sigma}_{\Delta U_{s-s}}$. The first three quantities enter in the misfit-only theory, and methods to compute them have been discussed and demonstrated in several alloy systems [13, 24]. Hence, we discuss in detail only the determination of $\widetilde{\sigma}_{\Delta U_{s-s}}$ in the next section.

## 4. Theory inputs

The inputs for the extended theory are derived from experiments where available. Otherwise, we compute them from DFT. The details of the DFT methodology employed here can be found in the Appendix.

### 4.1. Misfit volumes $\Delta V_n$

Misfit volumes in any solid-solution alloy are determined based on the derivatives of the alloy atomic volume with respect to the compositions as

$$\Delta V_n = \frac{\partial V_{\text{alloy}}}{\partial c_n} - \sum_{m=1}^{N} c_m \frac{\partial V_{\text{alloy}}}{\partial c_m}, \tag{10}$$

where $V_{\text{alloy}} = V_{\text{alloy}}(c_1, c_2, ..., c_{N-1})$ is a function of $N - 1$ independent solute concentrations and then $\partial V_{\text{alloy}}/\partial c_N = 0$ [24]. The lattice constants of $\text{Au}_{1-x}\text{Ni}_x$ with $x = 0.4$–$0.64$ have been measured in experiments [25] and the alloy atomic volumes can then be fit by linear regression as $V_{\text{alloy}} = -6.043c_{\text{Ni}} + 17.161$. These results yield a lattice constant of AuNi as 3.839 Å that agrees very well with our measured value (3.840 Å). More importantly, the misfit volumes of Au and

5

Ni in AuNi are determined as $\Delta V_{\text{Au}} = 3.022$ Å$^3$ and $\Delta V_{\text{Ni}} = -\Delta V_{\text{Au}}$.

The experimental misfit volumes lead to a misfit parameter $\delta = 7.116\%$. This is very large compared to many other fcc alloys [14] but is fully expected due to the large difference between the elemental lattice constants. In spite of the large misfit parameter, AuNi maintains a solid solution structure when fabricated as described here. The misfit parameter alone is thus not sufficient to assess whether an alloy can be fabricated as a solid solution.

### 4.2. Elastic constants $C_{ij}$

The experimental single-crystal elastic constants are not available for AuNi. We thus compute the $C_{ij}$ from DFT, using special quasi-random structures [26] and the stress-strain method [27]. For a given exchange-correlation functional, the accuracy of the predicted lattice and elastic constants are usually correlated, i.e. an overestimation of the lattice constant is usually accompanied by an underestimation of the elastic constants, and vice versa (see Appendix). Since the experimental lattice constant of AuNi is approximately the average of the PBEsol and PBE values, we assume that the true elastic constants $C_{ij}$ are close to the average of the PBEsol and PBE values, yielding $C_{11} = 199.6$ GPa, $C_{12} = 157.9$ GPa, and $C_{44} = 56.4$ GPa, with a Zener anisotropy index $A = 2.7$.

To validate the accuracy of these DFT-estimated $C_{ij}$, we use them to compute the polycrystalline Young's modulus using the Voigt-Reuss-Hill average. The predicted value is 106 GPa, in good agreement with the experimentally measured value (101 GPa). Hence, we use the PBEsol and PBE averaged $C_{ij}$ in making strength predictions.

### 4.3. Energy fluctuation $\widetilde{\sigma}_{\Delta U_{s-s}}$

Recalling that $\widetilde{\sigma}_{\Delta U_{s-s}}$ is the energy fluctuation associated with slip by a Shockley partial Burgers vector, this energy quantity is thus related to fluctuations in the SF energy. The computation of the SF energy is accomplished using the "tilted-cell" method [28]. For an fcc crystal, we first create a random atomistic realization of the alloy in a periodic cuboidal simulation cell defined by vectors $N_1\langle\frac{1}{2}\frac{1}{2}0\rangle \times N_2\langle\frac{1}{2}\frac{1}{2}1\rangle \times N_3\langle111\rangle$, denoted as dimension $N_1 \times N_2 \times N_3$ in the following. For a cross-sectional area $A_{\text{slip}}$ of the {111} plane, there are $N_{\text{slip}} = \frac{2A_{\text{slip}}}{\sqrt{3}b^2} = 2N_1N_2$ atoms in each atomic layer parallel to the slip plane. Then the out-of-plane lattice is tilted by the Shockley partial Burgers vector to initiate the SF. After relaxations, the total energy change

$\Delta U_{s-s}$ due to the imposed slip is calculated. This process is repeated many times for different random realizations to obtain a distribution of $\Delta U_{s-s}$ with mean $\langle\Delta U_{s-s}\rangle$ and standard deviation $\sigma_{\Delta U_{s-s}}$. Two intrinsic (size-independent) quantities emerge as

$$\langle\gamma\rangle = \langle\Delta U_{s-s}\rangle/A_{\text{slip}},$$
$$\widetilde{\sigma}_{\Delta U_{s-s}} = \sigma_{\Delta U_{s-s}}/\sqrt{N_{\text{slip}}}. \tag{11}$$

Here, $\langle\gamma\rangle$ is the average SF energy of the alloy, and $\widetilde{\sigma}_{\Delta U_{s-s}}$ is the intrinsic fluctuations of the SF energy that gives rise to extra strengthening.

For DFT calculations, PBEsol and PBE functionals lead to similar SF energies for pure Au and Ni (see Appendix). Hence, we use PBEsol to compute $\Delta U_{s-s}$ for the AuNi alloy. We use a supercell dimension $4 \times 2 \times 2$, i.e., 16 atoms per layer $\times$ 6 layers with $a = 3.810$ Å (PBEsol value). 90 random realizations of the bulk structure are created at the exact composition, where half of the sites are randomly selected and populated with Au atoms. For each bulk realization, the initial energy and the energy of the system after tilting are computed. Atoms are fully relaxed with the force convergence criterion of 10 meV/Å while holding the supercell lattices fixed to mimic the coherent lattice in the homogeneous random alloys. The standard calculation of the stable SF energy involves the relaxations of the stress components on the slip plane [28]. But for fcc metals, the inelastic normal displacements associated with this relaxation are usually small and decrease the energy only slightly [29]. Since this relaxation is computationally very expensive but with very small changes in energy, we do not relax the out-of-plane lattice in our calculations here. Our results thus slightly overestimate $\langle\gamma\rangle$ (by a few mJ/m$^2$) as compared to the fully-relaxed DFT calculations. This should also have a negligible effect on the standard deviation and thus on $\widetilde{\sigma}_{\Delta U_{s-s}}$.

The convergence of $\langle\gamma\rangle$ and $\widetilde{\sigma}_{\Delta U_{s-s}}$ with respect to the number of random realizations are shown in Fig. 5. The average SF energy $\langle\gamma\rangle$ converges to 112 mJ/m$^2$ after $\sim$ 50 realizations, as shown in Fig. 5a. Although slightly overestimated due to the lack of lattice relaxation, the converged SF energy is only modestly higher than the DFT average of the constituent elements (see Appendix). The standard deviation $\widetilde{\sigma}_{\Delta U_{s-s}}$ also converges but more slowly, ranging between 0.05 and 0.06 eV, as shown in Fig. 5b, and reaching 0.054 eV after 90 random realizations.

To further validate the DFT results of the SF structure (partial slip), we perform similar calculations for the full slip process, as also shown in Fig. 5. Full slip
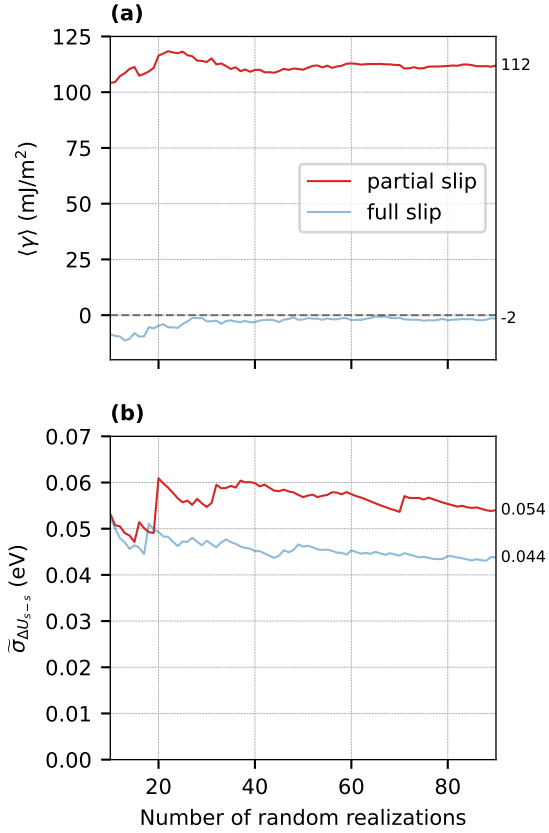
Figure 5: The convergences of the average stacking fault energy $\langle \gamma \rangle$ and the intrinsic energy fluctuation $\widetilde{\sigma}_{\Delta U_{s-s}}$ are examined as a function of the number of random realizations.

restores the bulk structure, so $\langle \gamma \rangle = 0$ is expected, and calculations reach $-2$ mJ/m$^2$ (see Fig. 5a). This consistency indicates that (i) the supercell size of 6 {111} layers, (ii) the force convergence criterion of 10 meV/Å, and (iii) the k-mesh density of $2\pi/50$ Å$^{-1}$, are sufficient to achieve good accuracy. In addition, the energy fluctuation $\widetilde{\sigma}_{\Delta U_{s-s}}$ for full slip converges to a value of 0.044 eV (see Fig. 5b). The similar values of $\widetilde{\sigma}_{\Delta U_{s-s}}$ for partial slip and full slip are not surprising, being consistent with analytic expressions for $\widetilde{\sigma}_{\Delta U_{s-s}}$ derived in terms of solute-solute effective pair interactions [18].

Moreover, a new neural-network interatomic potential (NNP) is fitted to DFT data in AuNi [30]. With more random realizations ($\sim 10^3$) and larger cell size ($\sim 10^3$ atoms), the NNP predicts a fully converged $\widetilde{\sigma}_{\Delta U_{s-s}}$ as 0.052 eV for partial slip, which is very close to our DFT result here. Hence, we will use the DFT result of $\widetilde{\sigma}_{\Delta U_{s-s}} = 0.054$ eV in the following strength prediction. Small changes to $\widetilde{\sigma}_{\Delta U_{s-s}}$ have very small effects on the alloy strength.

## 5. Strength predictions

To apply the misfit-only theory, we first examine the predicted partial separation $d_{\text{partial}}$. The Stroh formalism for anisotropic elasticity [31] predicts $d_{\text{partial}} = K_{12}/\langle \gamma \rangle$, where $K_{12}$ is an elastic prefactor. Using the lattice and elastic constants for AuNi, we obtain $K_{12} = 0.096$ eV/Å. With $\langle \gamma \rangle = 112$ mJ/m$^2$, the partial separation is then estimated as $5.1b$. This value is slightly lower than $6.5b$, above which the prefactors in Eq. 7 are independent of $d_{\text{partial}}$. However, the elemental benchmarks (see Appendix) show that the DFT SF energy of Ni is $\sim 25\%$ higher than the experiments. Hence, the as-computed $\langle \gamma \rangle$ here for AuNi is expected to be higher than the true experimental value. The true partial separation in AuNi should then be larger than predicted here, approaching or exceeding the requirement needed to apply the analytic theory. Otherwise, the value of $\langle \gamma \rangle$ does not enter the theory. We will thus make predictions using the results in Section 3.

With all the material parameters summarized in Table 1, the misfit-only yield stress of random AuNi at room temperature $T = 300$ K and strain rate $\dot{\varepsilon} = 10^{-3}$ s$^{-1}$ is predicted to be 714 MPa, as shown in Table 1. This value is only slightly lower ($-7\%$) than the experimental value of 769 MPa, and so is in agreement at a level comparable to other applications of the theory to fcc HEAs. The misfit contribution to strengthening is thus a large fraction of the experimental strength. The predicted misfit strengthening is significantly larger than those predicted for many other HEAs studied to date. For instance, the "high" strengths of NiCoV [32], Ni$_{63.2}$V$_{36.8}$ [33], and CoCrFeNiPd [16] are around 400 MPa [14, 15].

We now add the solute-solute contribution. The relevant computed values are shown in Table 1, in particular we have $\widetilde{\sigma}_{\Delta U_{s-s}} = 0.054$ eV, $\Delta \widetilde{E}_{p,s-d}(w_c) = 0.557$ eV, and hence $R_{ss/sd} = 0.412$. The scaled energy barrier and zero-temperature shear yield stress are then obtained, leading to a strength prediction under experimental conditions of 809 MPa (see Table 1). The increase due to solute-solute interactions is moderate ($+13\%$) but not negligible. The prediction is now slightly higher than, but closer to experiments (769 MPa). We consider this level of agreement made with a parameter-free model to be very good.

Examining some of the minor details that lead to the final predictions, some aspects suggest slight overprediction of the theory. For instance, the elastic moduli lead to a Young's modulus slightly higher than estimated experimentally, which may be due in part to finite-temperature reductions in the elastic moduli rel-

Table 1: Material parameters of AuNi and the strength predictions at temperature $T$ = 300 K and loading strain rate $\dot{\varepsilon}$ = $10^{-3}$ s$^{-1}$. The experimental yield strength is listed for comparison.

| Material parameters | | | | | | Theory predictions | | | Exp |
|---|---|---|---|---|---|---|---|---|---|
| $a$ (Å) | $C_{11}$ (GPa) | $C_{12}$ (GPa) | $C_{44}$ (GPa) | $\delta$ (%) | $\widetilde{\sigma}_{\Delta U_{s-s}}$ (eV) | $\Delta\widetilde{E}_{p,s-d}(w_c)$ (eV) | $\sigma_{y,s-d}$ (MPa) | $\sigma_y$ (MPa) | $\sigma_y$ (MPa) |
| 3.840 | 199.6 | 157.9 | 56.4 | 7.116 | 0.054 | 0.557 | 714 | 809 | 769 ± 4 |

ative to the 0 K DFT-calculated values. Another uncertainty arises due to the possible overestimation of the DFT-computed $\widetilde{\sigma}_{\Delta U_{s-s}}$. As mentioned, the DFT SF energy of pure Ni is notably higher than in experiments. These various effects should tend to reduce the predictions modestly, making them closer to experiments. At the same time, any grain-size Hall-Petch strengthening would imply that the intrinsic alloy strength is lower than the measured value, but the Hall-Petch effects here are likely to be small. The Hall-Petch scaling is not yet available for AuNi. Taking the scaling of Au-NiPdPtCu (675 MPa·$\mu$m$^{1/2}$ [34]) for rough estimation, the grain size of 60 $\mu$m would lead to a grain-boundary strengthening of only 87 MPa. However, the scalings of the constituent elements are much smaller, 80 and 230 MPa·$\mu$m$^{1/2}$ for Au and Ni [35], respectively, so any grain size effect could be much smaller.

Although chemical ordering to some degree is inevitable in reality, predictions for the random alloy remain extremely valuable. Random alloy predictions can be easily used to guide efficient alloy design and as a reference prediction that can be compared with the experiment to assess whether other mechanisms, such as SRO, would make a quantitative difference in the strength (as done in Refs. [15, 24]). Within the present framework of a random alloy, the strength predictions of AuNi here are already very close to experiments. This suggests that the overall net effects of SRO on strengthening are also small. This is consistent with recent experiments on NiCoCr, which reported small [36] or no [37, 38] effects on strengthening in spite of other evidence of SRO. The quantitative prediction of SRO effects requires the application of new emerging theories [39, 40]. These theories indicate that SRO can even decrease strength, counter to the widespread assumption that SRO always increases strength [16]. This may rationalize the success of the random alloy theories and is clearly an important topic for future work.

## 6. Discussion

### 6.1. Solute-solute vs. misfit in strengthening

The modest contribution of solute-solute interactions here also rationalizes much of the previous success of the misfit-only theory. The solute-solute interactions in AuNi lead to phase separation at ∼ 1035 K. In the various Cantor family of alloys (Co-Cr-Fe-Ni-Mn-V), there is only possible evidence of some SRO at these temperatures, suggesting that the solute-solute interactions in those alloys are smaller than those in AuNi. The misfit parameters are also smaller but the elastic moduli are considerably higher, leading to net smaller values of $\Delta\widetilde{E}_{p,s-d}(w_c)$ in those alloys as compared to AuNi. Thus, there are factors suggesting a competition between decreasing and increasing effects of solute-solute interactions in the Cantor family of alloys. To our knowledge, there is no direct connection between solute misfit volumes and solute-solute interactions, and so each alloy family must be studied to determine the ratio $R_{ss/sd}$. Since solute-solute interactions become less important for strength as the misfit strengthening increases, the results here clearly support the application of the *analytic* misfit-only theory for preliminary but efficient guidance for alloy design to achieve high strengths.

It is useful to generally assess the role of $\widetilde{\sigma}_{\Delta U_{s-s}}$ in affecting strength predictions. $\widetilde{\sigma}_{\Delta U_{s-s}}$ enters the theory only as the ratio $R_{ss/sd}$, with barrier and strength then scaling as $\left[1 + R_{ss/sd}^2\right]$ to the 1/3 and 2/3 powers, respectively (see Eq. 9). Thus, even when $R_{ss/sd} = 1$, $\tau_{y0}$ increases by only a factor of 1.59. This is certainly not a small change, but such a level of solute-solute interactions is probably too large for alloys that can be fabricated in a solid-solution state (without phase separation or precipitation under processing temperatures and times). For the AuNi alloy, we find $R_{ss/sd} = 0.412$ such that $\tau_{y0}$ increases by a factor of only 1.11. Hence, solute-solute interactions might be important mainly for alloys with small size mismatch and typical moduli, where the misfit energy $\Delta\widetilde{E}_{p,s-d}(w_c)$ is low. But these alloys have low misfit strength, and so may be of much less interest and importance than higher-strength alloys. Hence, we again conclude that the search for strong alloys can focus on the misfit contributions.

### 6.2. Solute-solute interactions only

While we recommend focusing on the misfit contribution to strengthening for alloy designs, it remains interesting to consider the situation where there is essentially no misfit or solute-dislocation contribution at all,

8

i.e. $\Delta \widetilde{E}_{p,s-d} = 0$. Such a situation can arise in alloys such as fcc NiCo and AuAg where the constituent elements have nearly the same atomic volumes, and hence misfit volumes are negligible. We analyze this case here and present a new theory for strengthening in this limit.

Even when $\Delta \widetilde{E}_{p,s-d} = 0$, the general theory still applies but the scaling of various quantities is changed significantly. For $w < d_{\text{partial}}$, we have

$$
\begin{aligned}
\Delta \widetilde{E}_p(w) &\propto w^{1/2}, \\
\zeta_c(w) &\propto w, \\
\sigma_{\Delta U_{\text{tot}}}(\zeta_c(w), w) &\propto w, \\
\Delta E_{\text{tot}}(\zeta_c(w), w) &\propto w^0.
\end{aligned}
\tag{12}
$$

The last of these equations shows that the total energy reduction is independent of $w$. Hence, there is no characteristic waviness - all scales with $w < d_{\text{partial}}$ have the same energy decrease $\Delta E_{\text{tot}}$ as compared to the original long straight dislocation. Dislocations can thus become wavy at all scales $w < d_{\text{partial}}$. However, due to the use of the line tension approximation, the theory should be limited to $w > b$. For $w > d_{\text{partial}}$, the quantity in Eq. 1 is modified and the analysis becomes more complicated as it involves the $\widetilde{\sigma}_{\Delta U_{s-s}}$ from the full slip [18]. The following analysis is valid if the ratio between the fluctuations of full slip and partial slip is less than $\sqrt{2}$, which is expected to be true in most alloys. In this case, $\Delta E_{\text{tot}}(\zeta_c(w), w)$ increases monotonically with increasing $w$. Therefore, dislocations will become wavy only over scales $b < w < d_{\text{partial}}$, and all scales in this range are possible because $\Delta E_{\text{tot}}$ is a constant. A similar situation of a scale-independent total energy decrease was found previously in the solute strengthening of twinning dislocations in magnesium alloys [41].

Although there is no characteristic scale, each scale $w$ considered separately has an energy barrier and a zero-temperature shear yield stress that scale as

$$
\begin{aligned}
\Delta E_b &\propto w, \\
\tau_{y0} &\propto w^{-1}.
\end{aligned}
\tag{13}
$$

So, among all possible waviness configurations $b < w < d_{\text{partial}}$, the strength will be controlled by the scale requiring the highest shear stress at the experimentally-specified temperature and loading strain rate. The reason for this is as follows. At zero stress, a long dislocation will have all allowed scales of waviness. But with increasing stress, the waviness at those scales that can be overcome at that applied stress will vanish, leaving only the remaining "stronger" waviness scales. At the

yield stress, only the strongest scale will remain, which determines the strength.

Following from the above, the strength-controlling scale, labeled here as $w_c$, can be derived analytically as

$$
w_c = \max \left[ b, \min \left( w_{c1}, d_{\text{partial}} \right) \right],
\tag{14}
$$

where

$$
w_{c1}(T, \dot{\varepsilon}) = 1.11 \left[ \frac{\widetilde{\sigma}_{\Delta U_{s-s}}^2 \Gamma}{b^2} \right]^{-\frac{1}{3}} \left[ kT \ln \frac{\dot{\varepsilon}_0}{\dot{\varepsilon}} \right].
\tag{15}
$$

The associated uniaxial yield strength $\sigma_{y,s-s}(T, \dot{\varepsilon})$ is then computed at $w = w_c$. For $w_c = w_{c1}$, the strength is

$$
\sigma_{y,s-s}(T, \dot{\varepsilon}) = 2.80 \left[ \frac{\widetilde{\sigma}_{\Delta U_{s-s}}^2}{b^3} \right] \left[ kT \ln \frac{\dot{\varepsilon}_0}{\dot{\varepsilon}} \right]^{-1}.
\tag{16}
$$

This result, for computed $\widetilde{\sigma}_{\Delta U_{s-s}}$, is complementary to the misfit-only strengthening theory. Thus, we now have analytic theories for the two limiting cases (misfit-only and solute-solute-only), which should be of value as researchers assess different strengthening mechanisms.

As an example, applied to AuNi at the experimental conditions, we obtain $w_c = w_{c1} = 4.1b$. The strengthening due purely to the solute-solute interactions is then computed via Eq. 16 as $\sigma_{y,s-s} = 157$ MPa. This strength is much lower than the experimental strength (769 MPa), consistent with the dominance of misfit strengthening in the AuNi alloy.

### 6.3. Computational methods for $\widetilde{\sigma}_{\Delta U_{s-s}}$

We have shown that the solute-solute quantity $\widetilde{\sigma}_{\Delta U_{s-s}}$ entering the theory can be computed directly in DFT using the standard method for computing SF energies. However, standard DFT methods (e.g. VASP with PBEsol or PBE and collinear spin-polarization) themselves can be imperfect tools for computing energies in random alloys [24]. In particular, in magnetic systems that are much more complex than AuNi, there can be spin flips occurring between the bulk and SF configurations that may not be realistic but contribute additional (spurious) fluctuations in the computed $\widetilde{\sigma}_{\Delta U_{s-s}}$.

In the absence of possible spurious computational effects, DFT computations of $\widetilde{\sigma}_{\Delta U_{s-s}}$ require a sufficient cell size and sufficient sampling of the configurational space to achieve accurate values. This is computationally very expensive. We will thus report in future work [30] on the alternative approach of using a database of small-cell DFT energies to develop a

9

machine-learned interatomic potential that is both accurate and efficient, greatly facilitating the computation of a converged value of $\widetilde{\sigma}_{\Delta U_{s-s}}$. A second related approach to compute $\widetilde{\sigma}_{\Delta U_{s-s}}$ is to use DFT to compute solute-solute effective pair interactions (EPIs) [18]. Due to the large size misfit and significant local atomic relaxations that are caused, AuNi is an extreme system where the standard cluster expansion method (in terms of pairs, triplets, etc.) might be especially inaccurate for energy predictions [42]. The accuracy of EPI-based $\widetilde{\sigma}_{\Delta U_{s-s}}$ and the consequent strength predictions will also be examined in future work [30].

## 7. Conclusions

We quantitatively investigate the role of misfit strengthening and solute-solute strengthening in AuNi as a test of theoretical models. Experimentally, AuNi samples are fabricated, characterized, and tested systematically to provide a clean basis for testing theory. The theory focuses on the role of solute-solute interactions, as captured through the intrinsic energy fluctuation $\widetilde{\sigma}_{\Delta U_{s-s}}$ associated with slip, as an additional contribution to strengthening beyond the solute misfits. The theory is then framed in a very convenient analytic form suitable for all fcc alloys. The value of $\widetilde{\sigma}_{\Delta U_{s-s}}$ in AuNi is then computed directly by sampling the stacking fault energies in DFT. Together with other material parameters entering the theory, we predict the strengthening of a random AuNi alloy without and with the solute-solute contributions. Both predictions are in good agreement with experiments, with the misfit contribution dominating and solute-solute contribution being moderate (+13%). We have discussed aspects of the theory, including the strengthening in the limiting case where the misfit effects are zero. The general theory, validated here with experiments on AuNi, is thus useful for broader applications to the computationally-guided design of high-performance complex alloys.

## Appendix

*DFT methodology for Au-Ni*

Spin-polarized DFT computations as implemented in the VASP code [47] are performed with both the PBEsol [48] and PBE [49] exchange-correlation functionals and the PAW pseudopotentials [50]. The valence-electron eigenstates are expanded using a plane wave basis set with a cutoff energy of 550 eV and smeared using the first-order Methfessel-Paxton method [51] with a smearing parameter of 0.2 eV. In reciprocal space, a Γ-centered Monkhorst-Pack k-mesh [52] is used with line density ($2\pi/50$ Å$^{-1}$) consistent across all geometries. This k-mesh density leads to, for example, $12 \times 12 \times 12$ for Au and $14 \times 14 \times 14$ for Ni in the fcc cubic unit cells. Unless indicated, the ionic forces are relaxed to $< 1$ meV/Å in ionic relaxations.

*DFT results of elemental benchmarks*

We start with the elemental benchmarks for Au and Ni, as presented in Table 2. Our elemental DFT results are broadly consistent with the literature [53, 54]. The lattice constant $a$ and the bulk modulus $B$ are extracted from the equation of state energy-volume calculations. The "standard" stable SF energy $\gamma$ is calculated using the standard tilted-cell method [28], where (i) the in-plane lattices are fixed according to the equilibrium bulk value, (ii) the out-of-plane lattice is fully relaxed to release the supercell stress $\sigma_{3j}$ ($j = 1, 2, 3$), and (iii) all the atoms are fully relaxed. The supercell consists of 1 atom per layer $\times$ 6 layers.

To further validate the results of $\gamma$, we take the "standard" set as the starting point and tweak a few DFT parameters. The "box-fixed" set is computed with the supercell lattices fixed during ionic relaxations, as applied in the AuNi alloy in Section 4. "L12" denotes 12 {111} layers instead of 6. "K100" means the k-point line interval is $2\pi/100$ Å$^{-1}$, which is half of that in the "standard" set and leads to $\sim$ 8 times more irreducible k-points in the calculations.

Table 2: The elemental benchmarks of Au and Ni. RT = room temperature. Please see text for details.

| | | | $a$ (Å) | $B$ (GPa) | $\gamma$ (mJ/m$^2$, Shockley partial slip) | | | | $\gamma$ (mJ/m$^2$, full slip) |
|---|---|---|---|---|---|---|---|---|---|
| | | | | | standard | box-fixed | L12 | L12+K100 | box-fixed |
| Au | Exp | RT | 4.077[a] | 175[a] | 33[c] | | | | |
| | | 0 K | 4.065[b] | 180[a] | - | | | | |
| | DFT | PBEsol | 4.080 | 177 | 44 | 45 | 41 | 32 | 6.5 |
| | | PBE | 4.157 | 138 | 40 | | | | |
| Ni | Exp | RT | 3.525[a] | 184[a] | 125 ± 5[d] | | | | |
| | | 0 K | 3.515[a] | 188[a] | - | | | | |
| | DFT | PBEsol | 3.462 | 228 | 155 | 155 | 153 | 155 | 0.2 |
| | | PBE | 3.517 | 195 | 149 | | | | |

[a] Simmons et al., 1971 [43].
[b] Pamato et al., 2018 [44].
[c] Balk et al., 2001 [45].
[d] Carter et al., 1977 [46].

Overall, *pure Au* needs an extremely dense k-mesh to get a fully converged SF energy within the tilted-cell method (e.g., $40 \times 40 \times 4$ in the "L12+K100" case). A similar issue was also observed in pure Cu, which is in the same group as Au. To further validate, we compute the full slip process with the "box-fixed" settings, where the tilted structure is exactly the same as the pristine one. However, for Au, the two energies have a difference of $\sim 3$ meV (6.5 mJ/m$^2$), indicating insufficient DFT parameters (k-mesh density specifically). On the other hand, Ni converges very well. The resulting 0.2 mJ/m$^2$ corresponds to an energy difference of $\sim 0.1$ meV (for 6 atoms), which is close to the limit of DFT precision. Hence, the examination of the full slip is useful, i.e., if the full slip $\gamma$ turns out to be 0, then the DFT parameters are probably sufficient. We apply this to examine the AuNi alloy in the main text (see Fig. 5a).

*DFT results of AuNi: basic properties*

For AuNi alloy, the PBEsol energies of various AuNi systems including ordered and disordered structures agree well with literature calculations, e.g., the LDA [55] results in Ref. [56] (Fig. 11). However, the lattice constant of AuNi random alloy is calculated using PBEsol as 3.810 Å and using PBE as 3.876 Å. The errors are $-0.8\%$ and $+0.9\%$, respectively, as compared to the room temperature experiments. These differences can be rationalized based on the elemental benchmarks for the exchange-correlation functionals. As shown in Table 2, the PBEsol functional predicts the lattice constants of Au and Ni with errors of $+0.4\%$ and $-1.5\%$. On the other hand, the PBE functional predicts the lattice constants of Au and Ni with errors of $+2.3\%$ and $+0.1\%$. So, the alloy lattice constants are underestimated using PBEsol and overestimated using PBE. The average of the PBEsol and PBE lattice constants is,

however, in rather good agreement with the experimental value.

The analysis above also implies that DFT overestimates the misfit volumes in AuNi, with either PBEsol or PBE. While we use the experimental values in predictions, it is useful to assess the accuracy of DFT estimates of the misfit volumes since experiments may not be available in many new proposed alloy systems. We thus performed DFT-PBEsol computations of the misfit volumes [13]. Special quasi-random structures [26] around the central composition (50–50) are created and their equilibrium volumes are computed. The misfit volume of AuNi is then computed using Eq. 10, yielding $\Delta V_{Au} = 3.140$ Å$^3$. This is only a slight overestimate of the experimental value, and so provides some support for the use of DFT for systems where the predicted elemental lattice constants are within $\sim 1.5\%$ of the experimental values.

Overall, for AuNi, all the DFT benchmarks here are in generally good agreement with experiments, which supports the usage of DFT in the study of the AuNi alloy.

## References

[1] E. George, W. Curtin, C. Tasan, High entropy alloys: A focused review of mechanical properties and deformation mechanisms, Acta Materialia 188 (2020) 435–474. URL: https://linkinghub.elsevier.com/retrieve/pii/S1359645419308444. doi:10.1016/j.actamat.2019.12.015.

[2] E. P. George, D. Raabe, R. O. Ritchie, High-entropy alloys, Nature Reviews Materials 4 (2019) 515–534. URL: http://www.nature.com/articles/s41578-019-0121-4. doi:10.1038/s41578-019-0121-4.

[3] W. A. Curtin, S. I. Rao, C. Woodward, Progress and challenges in the theory and modeling of complex concentrated alloys, MRS Bulletin 47 (2022) 151–157. URL: https://link.springer.com/10.1557/s43577-022-00306-5. doi:10.1557/s43577-022-00306-5.

[4] S. Gorsse, D. B. Miracle, O. N. Senkov, Mapping the world of complex concentrated alloys, Acta Materialia 135 (2017) 177–187. URL: https://linkinghub.elsevier.com/retrieve/pii/S1359645417305025. doi:10.1016/j.actamat.2017.06.027.

[5] C. Varvenne, A. Luque, W. A. Curtin, Theory of strengthening in fcc high entropy alloys, Acta Materialia 118 (2016) 164–176. URL: https://linkinghub.elsevier.com/retrieve/pii/S1359645416305481. doi:10.1016/j.actamat.2016.07.040.

[6] C. Varvenne, G. Leyson, M. Ghazisaeidi, W. Curtin, Solute strengthening in random alloys, Acta Materialia 124 (2017) 660–683. URL: https://linkinghub.elsevier.com/retrieve/pii/S1359645416307455. doi:10.1016/j.actamat.2016.09.046.

[7] G. P. M. Leyson, W. A. Curtin, L. G. Hector, C. F. Woodward, Quantitative prediction of solute strengthening in aluminium alloys, Nature Materials 9 (2010) 750–755. URL: https://www.nature.com/articles/nmat2813. doi:10.1038/nmat2813.

[8] G. Leyson, L. Hector, W. Curtin, Solute strengthening from first principles and application to aluminum alloys, Acta Materialia 60 (2012) 3873–3884. URL: https://linkinghub.elsevier.com/retrieve/pii/S1359645412002273. doi:10.1016/j.actamat.2012.03.037.

[9] C. Varvenne, W. A. Curtin, Predicting yield strengths of noble metal high entropy alloys, Scripta Materialia 142 (2018) 92–95. URL: https://linkinghub.elsevier.com/retrieve/pii/S1359646217304943. doi:10.1016/j.scriptamat.2017.08.030.

[10] C. Varvenne, W. A. Curtin, Strengthening of high entropy alloys by dilute solute additions: CoCrFeNiAl and CoCrFeNiMnAl alloys, Scripta Materialia 138 (2017) 92–95. URL: https://linkinghub.elsevier.com/retrieve/pii/S1359646217302877. doi:10.1016/j.scriptamat.2017.05.035.

[11] G. Laplanche, J. Bonneville, C. Varvenne, W. Curtin, E. George, Thermal activation parameters of plastic flow reveal deformation mechanisms in the CrMnFeCoNi high-entropy alloy, Acta Materialia 143 (2018) 257–264. URL: https://linkinghub.elsevier.com/retrieve/pii/S1359645417308637. doi:10.1016/j.actamat.2017.10.014.

[12] G. Bracq, M. Laurent-Brocq, C. Varvenne, L. Perrière, W. Curtin, J.-M. Joubert, I. Guillot, Combining experiments and modeling to explore the solid solution strengthening of high and medium entropy alloys, Acta Materialia 177 (2019) 266–279. URL: https://linkinghub.elsevier.com/retrieve/pii/S1359645419304240. doi:10.1016/j.actamat.2019.06.050.

[13] B. Yin, W. A. Curtin, First-principles-based prediction of yield strength in the RhIrPdPtNiCu high-entropy alloy, npj Computational Materials 5 (2019) 14. URL: http://www.nature.com/articles/s41524-019-0151-x. doi:10.1038/s41524-019-0151-x.

[14] B. Yin, F. Maresca, W. Curtin, Vanadium is an optimal element for strengthening in both fcc and bcc high-entropy alloys, Acta Materialia 188 (2020) 486–491. URL: https://linkinghub.elsevier.com/retrieve/pii/S1359645420300884. doi:10.1016/j.actamat.2020.01.062.

[15] B. Yin, W. A. Curtin, Origin of high strength in the CoCrFeNiPd high-entropy alloy, Materials Research Letters 8 (2020) 209–215. URL: https://www.tandfonline.com/doi/full/10.1080/21663831.2020.1739156. doi:10.1080/21663831.2020.1739156.

[16] Q. Ding, Y. Zhang, X. Chen, X. Fu, D. Chen, S. Chen, L. Gu, F. Wei, H. Bei, Y. Gao, M. Wen, J. Li, Z. Zhang, T. Zhu, R. O. Ritchie, Q. Yu, Tuning element distribution, structure and properties by composition in high-entropy alloys, Nature 574 (2019) 223–227. URL: http://www.nature.com/articles/s41586-019-1617-1. doi:10.1038/s41586-019-1617-1.

[17] Y. Hu, W. Curtin, Modeling of precipitate strengthening with near-chemical accuracy: case study of Al-6xxx alloys, Acta Materialia 237 (2022) 118144. URL: https://linkinghub.elsevier.com/retrieve/pii/S1359645422005250. doi:10.1016/j.actamat.2022.118144.

[18] S. Nag, W. A. Curtin, Effect of solute-solute interactions on strengthening of random alloys from dilute to high entropy alloys, Acta Materialia 200 (2020) 659–673. URL: https://linkinghub.elsevier.com/retrieve/pii/S135964542030608X. doi:10.1016/j.actamat.2020.08.011.

[19] J. Wang, X.-G. Lu, B. Sundman, X. Su, Thermodynamic assessment of the Au–Ni system, Calphad 29 (2005) 263–268. URL: https://linkinghub.elsevier.com/retrieve/pii/S0364591605000830. doi:10.1016/j.calphad.2005.09.004.

[20] J. Rodríguez-Carvajal, Recent advances in magnetic structure determination by neutron powder diffraction, Physica B: Condensed Matter 192 (1993) 55–69. URL: https://www.sciencedirect.com/science/article/pii/092145269390108I. doi:10.1016/0921-4526(93)90108-I.

[21] R. Labusch, A Statistical Theory of Solid Solution Hardening, physica status solidi (b) 41 (1970) 659–669. URL: https://onlinelibrary.wiley.com/doi/10.1002/pssb.19700410221. doi:10.1002/pssb.19700410221.

[22] G. Leyson, W. Curtin, Friedel vs. Labusch: the strong/weak pinning transition in solute strengthened metals, Philosophical Magazine 93 (2013) 2428–2444. URL: http://www.tandfonline.com/doi/abs/10.1080/14786435.2013.776718. doi:10.1080/14786435.2013.776718.

[23] S. Nag, C. Varvenne, W. A. Curtin, Solute-strengthening in elastically anisotropic fcc alloys, Modelling and Simulation in Materials Science and Engineering 28 (2020) 025007. URL: https://iopscience.iop.org/article/10.1088/1361-651X/ab60e0. doi:10.1088/1361-651X/ab60e0.

[24] B. Yin, S. Yoshida, N. Tsuji, W. A. Curtin, Yield strength and misfit volumes of NiCoCr and implications for short-range-order, Nature Communications 11 (2020) 2507. URL: http://www.nature.com/articles/s41467-020-16083-1. doi:10.1038/s41467-020-16083-1.

[25] Y. Vesnin, Y. Shubin, Equilibrium decomposition curve of Au-Ni solid solutions, Journal of the Less Common Metals 155 (1989) 319–326. URL: https://linkinghub.elsevier.com/retrieve/pii/0022508889902403. doi:10.1016/0022-5088(89)90240-3.

[26] A. Zunger, S.-H. Wei, L. G. Ferreira, J. E. Bernard, Special quasirandom structures, Physical Review Letters 65 (1990) 353–356. URL: https://link.aps.org/doi/10.1103/PhysRevLett.65.353. doi:10.1103/PhysRevLett.65.353.

[27] Y. Le Page, P. Saxe, Symmetry-general least-squares extraction of elastic data for strained materials from ab initio calculations of stress, Physical Review B 65 (2002) 104104. URL: https://link.aps.org/doi/10.1103/PhysRevB.65.104104. doi:10.1103/PhysRevB.65.104104.

[28] B. Yin, Z. Wu, W. Curtin, Comprehensive first-principles study of stable stacking faults in hcp metals, Acta Materialia 123 (2017) 223–234. URL: https://linkinghub.elsevier.

com/retrieve/pii/S1359645416308035. doi:10.1016/j.actamat.2016.10.042.

[29] P. Andric, B. Yin, W. Curtin, Stress-dependence of generalized stacking fault energies, Journal of the Mechanics and Physics of Solids 122 (2019) 262–279. URL: https://linkinghub.elsevier.com/retrieve/pii/S0022509618305751. doi:10.1016/j.jmps.2018.09.007.

[30] L. Li, B. Yin, in preparation (2023).

[31] Z. Wu, B. Yin, W. Curtin, Energetics of dislocation transformations in hcp metals, Acta Materialia 119 (2016) 203–217. URL: https://linkinghub.elsevier.com/retrieve/pii/S1359645416305808. doi:10.1016/j.actamat.2016.08.002.

[32] S. S. Sohn, A. Kwiatkowski da Silva, Y. Ikeda, F. Körmann, W. Lu, W. S. Choi, B. Gault, D. Ponge, J. Neugebauer, D. Raabe, Ultrastrong Medium-Entropy Single-Phase Alloys Designed via Severe Lattice Distortion, Advanced Materials 31 (2019) 1807142. URL: https://onlinelibrary.wiley.com/doi/10.1002/adma.201807142. doi:10.1002/adma.201807142.

[33] H. S. Oh, S. J. Kim, K. Odbadrakh, W. H. Ryu, K. N. Yoon, S. Mu, F. Körmann, Y. Ikeda, C. C. Tasan, D. Raabe, T. Egami, E. S. Park, Engineering atomic-level complexity in high-entropy and complex concentrated alloys, Nature Communications 10 (2019) 2090. URL: http://www.nature.com/articles/s41467-019-10012-7. doi:10.1038/s41467-019-10012-7.

[34] F. Thiel, D. Geissler, K. Nielsch, A. Kauffmann, S. Seils, M. Heilmaier, D. Utt, K. Albe, M. Motylenko, D. Rafaja, J. Freudenberger, Origins of strength and plasticity in the precious metal based high-entropy alloy AuCuNiPdPt, Acta Materialia 185 (2020) 400–411. URL: https://linkinghub.elsevier.com/retrieve/pii/S1359645419308493. doi:10.1016/j.actamat.2019.12.020.

[35] Z. C. Cordero, B. E. Knight, C. A. Schuh, Six decades of the Hall–Petch effect – a survey of grain-size strengthening studies on pure metals, International Materials Reviews 61 (2016) 495–512. URL: https://www.tandfonline.com/doi/full/10.1080/09506608.2016.1191808. doi:10.1080/09506608.2016.1191808.

[36] R. Zhang, S. Zhao, J. Ding, Y. Chong, T. Jia, C. Ophus, M. Asta, R. O. Ritchie, A. M. Minor, Short-range order and its impact on the CrCoNi medium-entropy alloy, Nature 581 (2020) 283–287. URL: http://www.nature.com/articles/s41586-020-2275-z. doi:10.1038/s41586-020-2275-z.

[37] K. Inoue, S. Yoshida, N. Tsuji, Direct observation of local chemical ordering in a few nanometer range in CoCrNi medium-entropy alloy by atom probe tomography and its impact on mechanical properties, Physical Review Materials 5 (2021) 085007. URL: https://link.aps.org/doi/10.1103/PhysRevMaterials.5.085007. doi:10.1103/PhysRevMaterials.5.085007.

[38] L. Li, Z. Chen, S. Kuroiwa, M. Ito, K. Kishida, H. Inui, E. P. George, Tensile and compressive plastic deformation behavior of medium-entropy Cr-Co-Ni single crystals from cryogenic to elevated temperatures, International Journal of Plasticity 148 (2022) 103144. URL: https://linkinghub.elsevier.com/retrieve/pii/S0749641921002126. doi:10.1016/j.ijplas.2021.103144.

[39] S. Nag, Concurrent multiscale modeling and theory of solute-strengthening for dilute and complex concentrated alloys, PhD thesis, EPFL, 2020. URL: https://doi.org/10.5075/epfl-thesis-7447.

[40] S. Nag, W. A. Curtin, Solute-strengthening in metal alloys with short-range order, submitted (2023).

[41] M. Ghazisaeidi, L. Hector, W. Curtin, Solute strengthening of twinning dislocations in Mg alloys, Acta Materialia 80 (2014) 278–287. URL: https://linkinghub.elsevier.com/retrieve/pii/S1359645414005631. doi:10.1016/j.actamat.2014.07.045.

[42] A. H. Nguyen, C. W. Rosenbrock, C. S. Reese, G. L. W. Hart, Robustness of the cluster expansion: Assessing the roles of relaxation and numerical error, Physical Review B 96 (2017) 014107. URL: http://link.aps.org/doi/10.1103/PhysRevB.96.014107. doi:10.1103/PhysRevB.96.014107.

[43] G. Simmons, H. Wang, Single Crystal Elastic Constants and Calculated Aggregate Properties. A Handbook, 2nd ed., The MIT Press, 1971.

[44] M. G. Pamato, I. G. Wood, D. P. Dobson, S. A. Hunt, L. Vočadlo, The thermal expansion of gold: point defect concentrations and pre-melting in a face-centred cubic metal, Journal of Applied Crystallography 51 (2018) 470–480. URL: https://scripts.iucr.org/cgi-bin/paper?S1600576718002248. doi:10.1107/S1600576718002248.

[45] T. J. Balk, K. J. Hemker, High resolution transmission electron microscopy of dislocation core dissociations in gold and iridium, Philosophical Magazine A 81 (2001) 1507–1531. URL: http://www.tandfonline.com/doi/abs/10.1080/01418610108214360. doi:10.1080/01418610108214360.

[46] C. B. Carter, S. M. Holmes, The stacking-fault energy of nickel, The Philosophical Magazine: A Journal of Theoretical Experimental and Applied Physics 35 (1977) 1161–1172. URL: https://www.tandfonline.com/doi/full/10.1080/14786437708232942. doi:10.1080/14786437708232942.

[47] G. Kresse, J. Furthmüller, Efficient iterative schemes for ab initio total-energy calculations using a plane-wave basis set, Physical Review B 54 (1996) 11169–11186. URL: https://link.aps.org/doi/10.1103/PhysRevB.54.11169. doi:10.1103/PhysRevB.54.11169.

[48] J. P. Perdew, A. Ruzsinszky, G. I. Csonka, O. A. Vydrov, G. E. Scuseria, L. A. Constantin, X. Zhou, K. Burke, Restoring the Density-Gradient Expansion for Exchange in Solids and Surfaces, Physical Review Letters 100 (2008) 136406. URL: https://link.aps.org/doi/10.1103/PhysRevLett.100.136406. doi:10.1103/PhysRevLett.100.136406.

[49] J. P. Perdew, K. Burke, M. Ernzerhof, Generalized Gradient Approximation Made Simple, Physical Review Letters 77 (1996) 3865–3868. URL: https://link.aps.org/doi/10.1103/PhysRevLett.77.3865. doi:10.1103/PhysRevLett.77.3865.

[50] G. Kresse, D. Joubert, From ultrasoft pseudopotentials to the projector augmented-wave method, Physical Review B 59 (1999) 1758–1775. URL: https://link.aps.org/doi/10.1103/PhysRevB.59.1758. doi:10.1103/PhysRevB.59.1758.

[51] M. Methfessel, A. T. Paxton, High-precision sampling for Brillouin-zone integration in metals, Physical Review B 40 (1989) 3616–3621. URL: https://link.aps.org/doi/10.1103/PhysRevB.40.3616. doi:10.1103/PhysRevB.40.3616.

[52] H. J. Monkhorst, J. D. Pack, Special points for Brillouin-zone integrations, Physical Review B 13 (1976) 5188–5192. URL: https://link.aps.org/doi/10.1103/PhysRevB.13.5188. doi:10.1103/PhysRevB.13.5188.

[53] A. Goyal, Y. Li, A. Chernatynskiy, J. S. Jayashankar, M. C. Kautzky, S. B. Sinnott, S. R. Phillpot, The influence of alloying on the stacking fault energy of gold from density functional theory calculations, Computational Materials Science

188 (2021) 110236. URL: https://linkinghub.elsevier.com/retrieve/pii/S0927025620307278. doi:10.1016/j.commatsci.2020.110236.

[54] X. Zhang, B. Grabowski, F. Körmann, A. V. Ruban, Y. Gong, R. C. Reed, T. Hickel, J. Neugebauer, Temperature dependence of the stacking-fault Gibbs energy for Al, Cu, and Ni, Physical Review B 98 (2018) 224106. URL: https://link.aps.org/doi/10.1103/PhysRevB.98.224106. doi:10.1103/PhysRevB.98.224106.

[55] D. M. Ceperley, B. J. Alder, Ground State of the Electron Gas by a Stochastic Method, Physical Review Letters 45 (1980) 566–569. URL: https://link.aps.org/doi/10.1103/PhysRevLett.45.566. doi:10.1103/PhysRevLett.45.566.

[56] C. Wolverton, V. Ozoliņš, A. Zunger, First-principles theory of short-range order in size-mismatched metal alloys: Cu-Au, Cu-Ag, and Ni-Au, Physical Review B 57 (1998) 4332–4348. URL: https://link.aps.org/doi/10.1103/PhysRevB.57.4332. doi:10.1103/PhysRevB.57.4332.